Chemical Science

ROYAL SOCIETY OF CHEMISTRY

EDGE ARTICLE

View Article Online
View Journal | View Issue

Check for updates

Cite this: *Chem. Sci.*, 2024, **15**, 765

Mn(III)-mediated carbon-centered radicals generate an enhanced immunotherapeutic effect†

Jiaxuan Li,‡[a] Baifei Hu,‡[b] Zelong Chen,‡[a] Jiahui Li,[a] Wenjuan Jin,[a] Yi Wang,[a] Yichen Wan,[a] Yinghua Lv,[a] Yuxin Pei,*[a] Hongtao Liu*[b] and Zhichao Pei*[a]

Received 14th July 2023
Accepted 5th December 2023

DOI: 10.1039/d3sc03635a

rsc.li/chemical-science

A strategy for designing cancer therapeutic nanovaccines based on immunogenic cell death (ICD)-inducing therapeutic modalities is particularly attractive for optimal therapeutic efficacy. In this work, a highly effective cancer therapeutic nanovaccine (denoted as MPL@ICC) based on immunogenic photodynamic therapy (PDT) was rationally designed and fabricated. MPL@ICC was composed of a nanovehicle of MnO_2 modified with a host–guest complex using amino pillar[6]arene and lactose-pyridine, a prodrug of isoniazid (INH), and chlorine e6 (Ce6). The nanovaccine exhibited excellent biosafety, good targeting ability to hepatoma cells and enrichment at tumor sites. Most importantly, it could modulate the tumor microenvironment (TME) to facilitate the existence of Mn(III) and Mn(III)-mediated carbon-centered radical generation with INH released from the prodrug *in situ* to further strengthen ICD. This is the first report on Mn(III)-mediated generation of carbon-centered radicals for successful anti-tumor immunotherapy using ICD, which provides a novel strategy for designing highly efficient cancer therapeutic nanovaccines.

Introduction

In recent years, cancer nanovaccine-based immunotherapy, due to its potential for high therapeutic efficacy, specificity, and ability to yield a long-term immune-memory effect, has exhibited promise to be one of the most effective ways of eradicating tumors and preventing tumor relapse, and alter the cancer treatment paradigm.[1] Cancer nanovaccines are nanoparticle-based vaccines, which can train and stimulate the immune system of the body to detect and eliminate tumors.[2] They can either consist of a careful combination of tumor antigens co-delivered with immunostimulatory adjuvants to induce potent T cell-mediated immune responses;[3] or they can induce immunogenic cell death (ICD) to boost tumor-associated antigen release, which provides *in situ* tumor vaccination to enhance the anti-tumor T cell response against primary tumor growth.[4] Research to date has indicated that several therapeutic modalities (such as chemotherapy,[5] radiotherapy,[6] phototherapy,[7] *etc.*) are capable of eliciting ICD, a special type of cell death that can activate antitumor immune responses.[8] However, ICD-mediated immunopotentiation achieved thus far is not sufficient for an ideal therapeutic result due to poor immunogenicity and the immunosuppressive tumor microenvironment (TME).[9] Considering the unique advantages of ICD-inducing modalities,[10] there is an urgent need to develop strategies to significantly increase their efficacy and durability, such as combining them with immune adjuvants and/or other ICD inducers. Adjuvants are indispensable components of vaccines that stimulate optimal immune responses towards non-replicating, inactivated, and subunit antigens.[11] In the search for adjuvants that can effectively activate cellular immunity, manganese oxide nanomaterials (MONs) have gained attention thanks to their unique physical and chemical properties, strengthening immunogenicity, modulation of the intrinsic TME, and excellent biodegradability and biosafety.[12] To date, the role of MONs in nanovaccines has been to induce ICD *via* Fenton-like reactions and ferroptosis.[13] The most common method is to utilize MnO_2 in chemodynamic therapy (CDT), where it is first reduced to Mn(II) in tumor cells by the high concentration of glutathione (GSH), and then produces reactive oxygen species (ROS) in the form of $^{\bullet}OH$ *via* a Mn(II)-mediated Fenton-like reaction. However, Mn(II)-mediated Fenton-like reactions rely on HCO_3^- and the prevalence of H_2O_2, which is reduced in tumor cells, thus limiting the immunotherapeutic effect of Mn(II).[14] Research has been conducted to mitigate these limitations, such as delivering HCO_3^- salt into tumor cells to accelerate the generation of $^{\bullet}OH$,[15] or by loading glucose oxidase into MONs to increase intracellular H_2O_2,[16] while still using Mn(II) as the catalyst. Notwithstanding the improvements made on the efficiency of Mn(II), it is known that different manganese valence states among oxides exhibit different levels of toxicity.[17] Compared with Mn(II), Mn(III), which is produced from MnO_2 through a single electron transfer (ET) process, has shown to be a stronger oxidant that can activate various organics

---

[a] *College of Chemistry & Pharmacy, Northwest A&F University, Yangling, Shaanxi 712100, P. R. China. E-mail: peiyx@nwafu.edu.cn; peizc@nwafu.edu.cn*

[b] *College of Basic Medical Sciences, Hubei University of Chinese Medicine, Huangjiahu West Road 16, Wuhan 430065, P. R. China. E-mail: hongtaoliu@hbtcm.edu.cn*

† Electronic supplementary information (ESI) available. See DOI: https://doi.org/10.1039/d3sc03635a

‡ These authors contributed equally to this work.

(phenol, fullerene, isoniazid, *etc.*) to generate carbon-centered radicals (˙R),[18] which are known to amplify ICD.[19] For instance, an enhanced tumor immunotherapy can be realized *via* the combination of AIPH (˙R producing reagent) and photothermal therapy (PTT) by triggering ˙R bursts.[20] Although Mn(III) has been identified to be a crucial component in certain reactions in biochemistry and bioinorganic chemistry,[21] Mn(III)-mediated ˙R has not yet been explored in cancer immunotherapy because of the instability of Mn(III) in an intrinsic TME due to its acidity.[22]

Photodynamic therapy (PDT), as a non-invasive and rapid tumor-ablation therapy, is one of the best candidates for constructing cancer therapeutic nanovaccines.[23] Tumors treated by PDT release tumor antigens, which act directly *in situ* as a patient-specific tumor vaccine.[24] However, the efficacy and immunity elicited by PDT alone are severely limited by the immunosuppressive TME, including the high concentration of GSH and the hypoxic environment.[25] Furthermore, the increased severity of hypoxia after PDT treatment, as a result of the photodynamic reactions, not only results in increased immunosuppression and impaired efficacy, but also causes rapid tumor recurrence.[26] Since MONs have the potential to reverse the immunosuppressive nature of the TME by increasing the pH, exhausting H_2O_2/GSH, and generating O_2,[17a] there is potential to combine PDT with MON-based platforms to improve ICD.

Taken together, we hypothesize that by rationally designing a MON-based nanoplatform utilizing MONs that would modulate the TME to improve the PDT induced ICD efficacy, as well as maximizing Mn(III)-mediated ˙R to further strengthen ICD, a highly effective cancer therapeutic nanovaccine can be achieved. Hence, as a proof of concept, we propose a cancer therapeutic nanovaccine (denoted as MPL@ICC) composed of an amino pillar[6]arene⊃lactose-pyridine modified hollow MnO_2 nanovehicle, INH-CA, a prodrug consisting of isoniazid (INH) protected by cinnamic aldehyde (CA), and chlorine e6 (Ce6), a photosensitizer (Scheme 1a). INH was chosen as it is known to generate ˙R when it reacts with Mn(III)[18c,27] and is already an FDA-approved drug commonly used against tuberculosis.[28] The use of INH in its prodrug state INH-CA should prevent the reaction between INH and MnO_2 before MPL@ICC enters tumor cells. After MPL@ICC enters tumor cells, MnO_2 will consume GSH and convert H_2O_2 to O_2, which triggers the release of INH-CA as well as Ce6. The acidic TME subsequently facilitates the rapid release of INH from INH-CA. INH and Ce6 then, together enhance the effect of PDT to induce ICD (Scheme 1b). In addition, the consumption of GSH and H_2O_2 by MnO_2 will increase the pH, which alters the TME to be more conducive for the existence of Mn(III). Subsequently, Mn(III) facilitates the generation of ˙R from INH to further potentiate immunogenic death of tumor cells.

Results and discussion

Before constructing the proposed nanovaccine, it was first necessary to confirm that the reaction between MnO_2 and INH

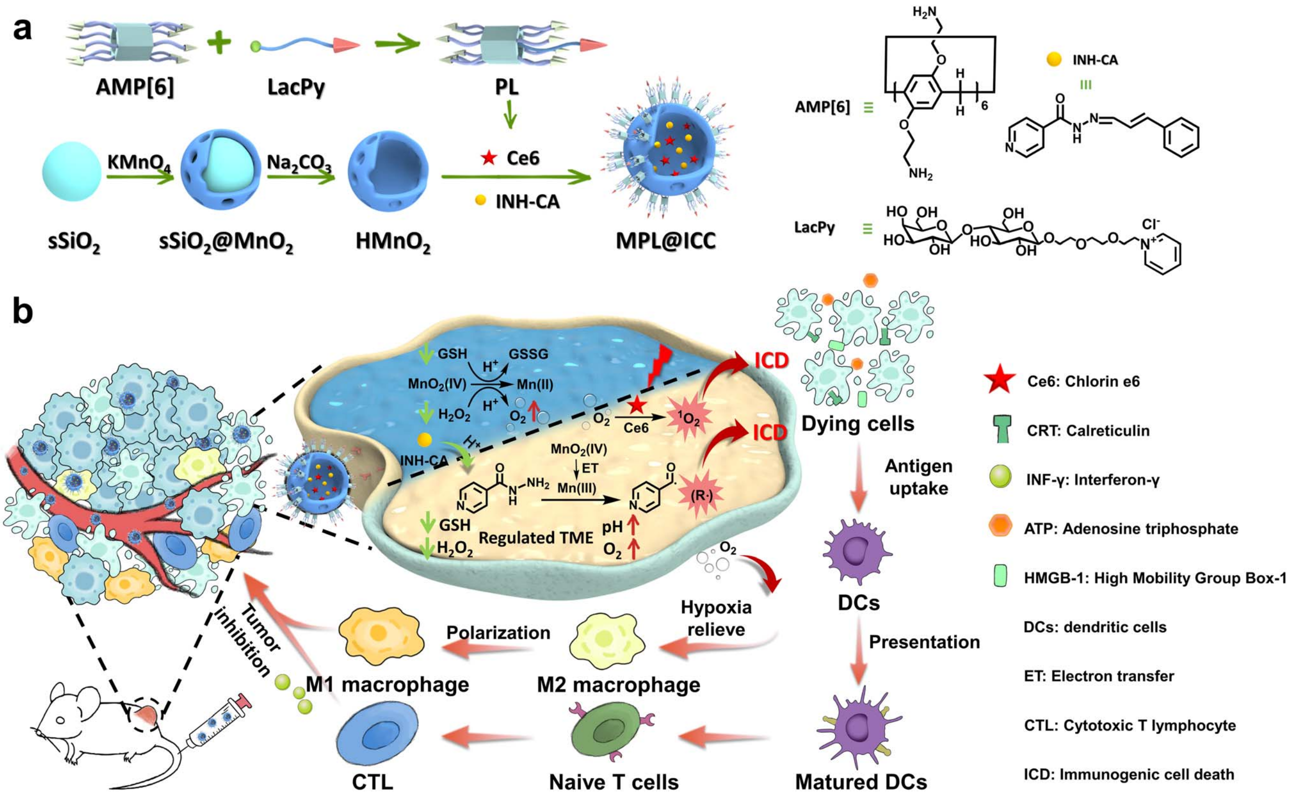

Scheme 1 (a) Scheme of the synthesis of the MPL@ICC nanovaccine. (b) Scheme of the nanovaccine used to induce ICD to elicit an anti-tumor immune response.

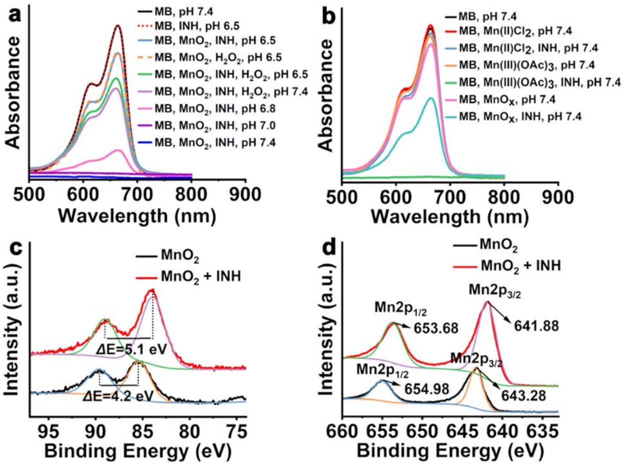

Fig. 1 (a) (b) UV-vis absorption spectra of MB after degradation in different solutions. (c) Mn 3s and (d) Mn 2p spectra of MnO_2 and MnO_2 + INH. MB: methylene blue; INH: isoniazid.

can produce $^{\bullet}$R through the Mn(III) intermediate. Theoretically, the spatial difference in the d_{z^2} and $d_{x^2-y^2}$ orbitals of Mn(IV) allows for a single electron transfer process during the reduction of Mn(IV).[22b,29] Although early studies indicated that MnO_2 can react with INH to produce $^{\bullet}$OH in tumor cells through non-Fenton-like reactions,[14b] a recent study demonstrated that in a buffer solution at pH 7.4, $^{\bullet}$R can also be generated in the same reaction.[27] It is therefore reasonable to hypothesize the formation of a Mn(III) intermediate in the reaction between MnO_2 and INH, which mediates the generation of $^{\bullet}$R. To confirm this, the free radical production in different solutions was determined using methylene blue (MB) as a probe (Fig. 1a). The degradation of MB caused only by INH is negligible in the pH range from 6.5 to 7.4 (Fig. S1†). While clear absorption decreases were observed in the solutions containing H_2O_2, interestingly, the absorption decreased slightly more when the pH rose from 6.5 to 7.4, which is less conducive to Mn(II)-mediated Fenton-like reactions, indicating another free radical production mechanism that requires a more basic condition is involved. Furthermore, the elimination of H_2O_2, which is crucial for Mn(II)-mediated Fenton-like reactions, resulted in the lowest absorption and thus the most free radical production, with the maximum production observed at pH 7.4.

Given that previous studies indicated that Mn(III) can react with INH to produce $^{\bullet}$R at pH 7.4, MnO_2 was replaced with Mn(II)Cl_2, Mn(III)$(OAc)_3$ and the precipitate that was collected after the reaction of MnO_2 with INH (denoted as MnO_X) to verify the reason for the MB oxidation observed under conditions not conducive to Mn(II)-mediated Fenton-like reactions (Fig. 1b). As expected, no significant decrease in MB absorbance was observed when Mn(II) was combined with INH at pH 7.4; when Mn(III) was combined with INH at pH 7.4, the MB absorbance completely disappeared, and an obvious decrease in absorption was observed when MnO_X was combined with INH at pH 7.4, further confirming the existence of a separate oxidation mechanism from the well-known Mn(II)-mediated Fenton-like reaction. Next, XPS was used to examine the precipitate that was collected after the reaction of MnO_2 with INH (Fig. 1c and d) in various solutions. The binding energy difference $\Delta E = 5.1$ eV in the Mn 3s spectrum of the precipitate indicates that the valence state of Mn was almost identical to that of MnOOH previously reported.[30] In the spectra of Mn 2p, the peaks located at 643.28 and 654.98 eV are attributed to the Mn $2p_{3/2}$ and Mn $2p_{1/2}$ for the MnO_2, which is in good agreement with the previous report on MnO_2.[31a] After reacting with INH, the two peaks shifted to 641.88 and 653.68 eV, respectively, which agrees well with that reported for MnOOH.[31b] This verifies the formation of Mn(III) from MnO_2 in the solutions, possibly through the ET process.[29,32] Having confirmed the presence of Mn(III) in the reactions, the $^{\bullet}$R generation of MnO_2 and INH under different conditions was studied by electron spin resonance (ESR) using 3,4-dihydro-2,3-dimethyl-2*H*-pyrrole 1-oxide (DMPO) (Fig. S2†). Although the generation of $^{\bullet}$OH from the Fenton-like reaction was observed at varying degrees in all but one solution (MnO_2, INH, pH 6.5) and control, no significant $^{\bullet}$R signal was observed. The difficulty in detecting $^{\bullet}$R through ESR is likely due to its instability, which leads to a low steady-state concentration that is difficult to be trapped by DMPO. However, the presence of $^{\bullet}$R self-quenching products was detected after the reaction between MnO_2 and INH using HRMS (Fig. S3 and S4†), which indicates the formation of $^{\bullet}$R in this reaction. These combined results strongly suggest that INH reduces Mn(IV) to Mn(III), and then Mn(III) catalyzes INH to generate carbon-centered free radicals, although the oxidized product of INH in the reduction step of Mn(IV) to Mn(III) by INH is not clear since it is very difficult to distinguish from that in the step of oxidation of INH by Mn(III) (Fig. S5†). This would provide an alternative and complementary pathway to Mn(II)-mediated Fenton-like reactions for MnO_2 to generate free radicals and more effectively kill tumor cells *via* ICD.

Having determined the potential of Mn(III) to generate $^{\bullet}$R for inducing ICD, MPL@ICC was fabricated. First, all the required compounds (amino pillar[6]arene (P), lactose-pyridine (L) and INH-CA) were synthesized according to the method as described in the ESI,† and characterized by NMR and HRMS (Fig. S6–S22†). Thereafter, the host–guest complexation between amino pillar[6]arene and lactose-pyridine was investigated by ^{1}H NMR. The chemical shift of pyridine protons clearly shifted to a high field due to the shielding effect of amino pillar[6]arene (Fig. S23†), which indicated the formation of a pillar[6]arene$\supset\star$ lactose-pyridine complex (PL). Using a Job's plot method, the stoichiometry of the PL complexation was determined to be 1 : 1 for amino pillar[6]arene$\supset$lactose-pyridine (Fig. S24†).

$HMnO_2$ was prepared according to a previously reported method.[12a,33] Transmission electron microscopy (TEM) images (Fig. 2a) clearly revealed the hollow structure of $HMnO_2$ and $HMnO_2$ modified with PL (MPL). The particle size of MPL (~170 nm) was observed to be significantly larger than that of $HMnO_2$ (~127 nm) due to the modification of PL onto the surface of $HMnO_2$, while the cavity sizes remained largely the same. Further, the hydrated particle size distribution of the different nanoparticles was analysed by dynamic light scattering (DLS). The $HMnO_2$ obtained after Na_2CO_3 etching had the largest particle size (average size = 1088 nm, PDI = 0.798), indicating

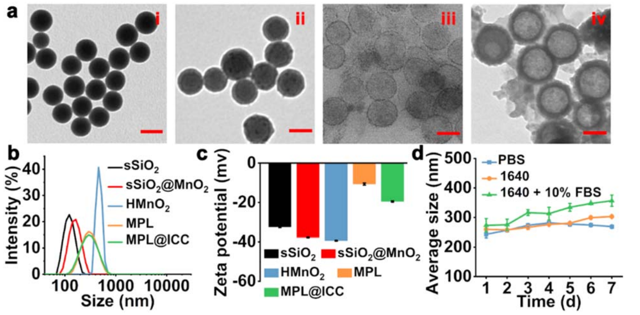

Fig. 2 (a) TEM images of (i) sSiO$_2$, (ii) sSiO$_2$@MnO$_2$, (iii) HMnO$_2$ and (iv) MPL. Scale bar: 100 nm. (b) The size distribution of different nanoparticles. (c) The zeta potential of different nanoparticles. (d) The stability of MPL@ICC within 7 days when stored in different solutions.

a significant aggregation due to the hydrophobic surface (Fig. 2b). After PL modification, the surface hydrophilicity of MPL significantly improved (average size = 259.5 nm, PDI = 0.172). The zeta potential of MPL rose to −10 ± 0.5 mV due to the presence of amino groups in P, which proves the successful modification of PL (Fig. 2c). Furthermore, the content of MnO$_2$ in MPL was determined to be 75.4 ± 2.3% by titration. Finally, the nanovaccine MPL@ICC (average size = 250.8 nm, PDI = 0.196) was obtained by loading photosensitizer Ce6 and INH-CA into MPL. The zeta potential of MPL@ICC rose further to −19.5 ± 0.3 mV, which may be attributed to the negative charge of Ce6. To verify its stability, MPL@ICC was added to different solutions (Fig. 2d). There was no obvious size change within 7 days (d) in PBS or 1640 culture medium, while the size gradually increased in FBS-containing 1640 medium after 2 days, which was attributed to the adsorption of proteins. These results indicate that MPL@ICC exhibits good stability and can be applied in further studies.

The characteristic peaks of Ce6 and INH-CA were observed in the UV-Vis absorption spectrum of MPL@ICC, indicating their successful encapsulation (Fig. S25a†). The drug loading capacity of MPL@ICC for Ce6 and INH-CA was measured using UV-Vis spectroscopy, which reached 32.4% and 17.6%, respectively (Fig. S26†). The release behavior of Ce6 and INH-CA from MPL@ICC was investigated through incubation in different solutions that mimic the TME for different lengths of time (Fig. S25b†). It was observed that drug release was significantly faster at pH 5.8 compared to pH 7.4. Furthermore, near complete drug release occurred in solutions containing 10 mM GSH after 8 h due to the rapid reduction of HMnO$_2$ by GSH. In addition, MPL was also shown to efficiently consume GSH in a concentration-dependent manner (Fig. S25c†). GSH causes a rapid release of INH-CA at the tumor site. The compound INH-CA constructed using an acid response Schiff base (Fig. S27†) can avoid the direct reaction of MnO$_2$ with INH. And INH was released from INH-CA *via* the acid responsive hydrazine bond linking INH to CA at the low pH of the TME, which happened before the pH of the TME was finally increased due to the consumption of GSH and H$_2$O$_2$ by MnO$_2$. The level of dissolved O$_2$ after adding different concentrations of MPL to a H$_2$O$_2$ solution (100 μM) was measured using an oxygen probe, which indicated a clear increase that was MPL concentration-dependent (Fig. S25d†). The photostability of MPL@ICC was studied *via* exposure to light irradiation for different durations (660 nm, 7 mW cm^{-2}) and the results are shown in Fig. S28.† Within 30 min, the maximum absorbance of MPL@ICC decreased only by 2.8% while that of free Ce6 decreased by 13.8%. This indicates that the loading of Ce6 in MPL@ICC increases the photostability of the photosensitizer (Fig. S28a†). In addition, the characteristic peak of Ce6 becomes broad and generates a bathochromic shift (Fig. S28b and c†). Furthermore, 1,3-diphenylisobenzofuran (DPBF) was used as a probe to detect the generation of singlet oxygen (^{1}O$_2$). As shown in Fig. S29,† both free Ce6 and MPL@ICC can effectively generate ^{1}O$_2$ under 660 nm laser irradiation (5 mW cm^{-2}), which is proven by the dramatically decreased absorption intensity of DPBF.

Following the successful fabrication of MPL@ICC, *in vitro* experiments were conducted to determine the targeting ability towards hepatoma cells. The modification of PL not only increases the size stability, but should mediate the endocytosis of the nanovaccine *via* specific interactions between the lactose units in L and lactose receptors (ASPRs) that are over-expressed on the surface of hepatoma cells.[34] To evaluate the targeting ability of MPL@ICC to hepatoma cells, the red fluorescence of Ce6 was observed by confocal laser scanning microscopy (CLSM) after MPL@ICC was incubated with different cell lines (Fig. 3a and c). The red fluorescence of HepG2 cells and H22 cells was significantly stronger than that of HL7702 cells and HeLa cells. In contrast, the fluorescence intensity of intracellular Ce6 was significantly weaker when the lactose receptors (ASPRs) of the cells were blocked by LBA or when HMnO$_2$ was used.

The ability of MPL@ICC to alleviate intracellular hypoxia was explored by using commercial hypoxia probe pimonidazole and the FITC-MAb1 antibody (Fig. 3b and d), where the cells under hypoxia would display bright green fluorescence. As expected, since MnO$_2$ in MPL or MPL@ICC generates O$_2$ by decomposing H$_2$O$_2$, the hypoxic state of the tumor cells was alleviated, leading to almost no observable green fluorescence. A GSH detection kit was used to detect the content of intracellular GSH after incubation with MPL to determine the GSH depletion capability of MPL@ICC. As shown in Fig. 3e, intracellular GSH was nearly depleted after 4 h incubation with MPL, and no recovery of the GSH-levels was observed after 12 h of incubation. These results demonstrate the strong depletion ability of MnO$_2$ for intracellular GSH.

The ability of MPL@ICC to induce oxidative stress in cells was explored by using 2′,7′-dichlorodihydrofluorescein diacetate (DCFH-DA) as a probe (Fig. 4a and b). Compared with the PBS group, the addition of MPL only produced weak green fluorescence due to the limited efficiency of the Mn(II)-mediated Fenton-like reaction. In contrast, MPL@INH-CA (MPL@IC) and MPL@ICC groups exhibited enhanced green fluorescence, which could be attributed to Mn(III)-mediated generation of $^\bullet$R. After 660 nm light irradiation, Ce6 was rapidly excited to generate ^{1}O$_2$, resulting in the observation of strong green fluorescence in the MPL@Ce6 + light group. Through the combined effect of ^{1}O$_2$ and $^\bullet$R, the MPL@ICC + light group displayed the

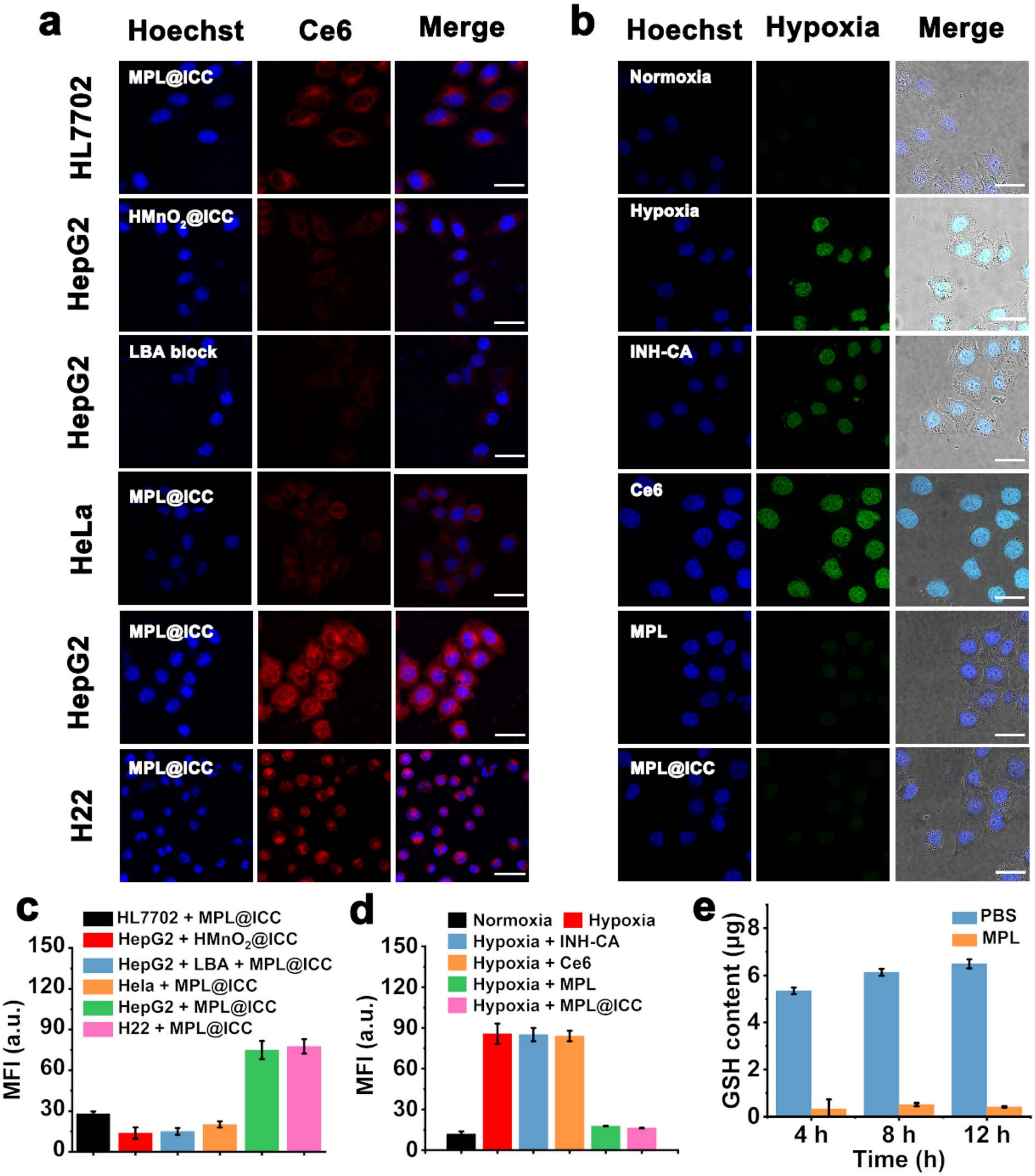

Fig. 3 (a) Confocal fluorescent microscopic images of different cells treated with MPL@ICC for 3 h (1×10^5 cells per dish, Hoechst 33258: Ex: 346 nm/Em: 460 nm; Ce6: Ex: 660 nm/Em: 710 nm). Scale bar: 30 μm. (b) The hypoxia detection of HepG2 cells cultured under different conditions for 3 h (1×10^5 cells per dish, pimonidazole as a hypoxia probe, FITC-labeled anti-pimonidazole antibody shows fluorescence. Ex: 488 nm/Em: 530 nm). Scale bar: 30 μm. (c) The mean fluorescence intensity of (a) ($n = 3$). (d) The mean fluorescence intensity of (b). (e) GSH content in HepG2 cells (1×10^7) after being cultured with MPL for different times ($n = 3$). Data are expressed as means ± SD.

strongest green fluorescence. Subsequently, the standard MTT assay was used to detect cell viability under different treatments. No decrease in cell viability was observed after co-incubating MPL with HL7702 cells, while the viability of HepG2 cells under the same conditions slightly decreased due to Mn(II)-mediated Fenton-like reactions (Fig. S30†). Neither free Ce6 nor MPL@Ce6 causes obvious damage to HepG2 cells in the dark. In contrast, a rapid decrease of HepG2 cell viability with increasing concentration of MPL@ICC was observed (Fig. 4c). After light irradiation, free Ce6 exhibited strong tumor cytotoxicity. Compared with free Ce6, MPL@Ce6 + light treatment showed higher cytotoxicity likely due to the enhanced cellular uptake of MPL@Ce6 and disruption of the redox balance caused by GSH depletion. As expected, the combined

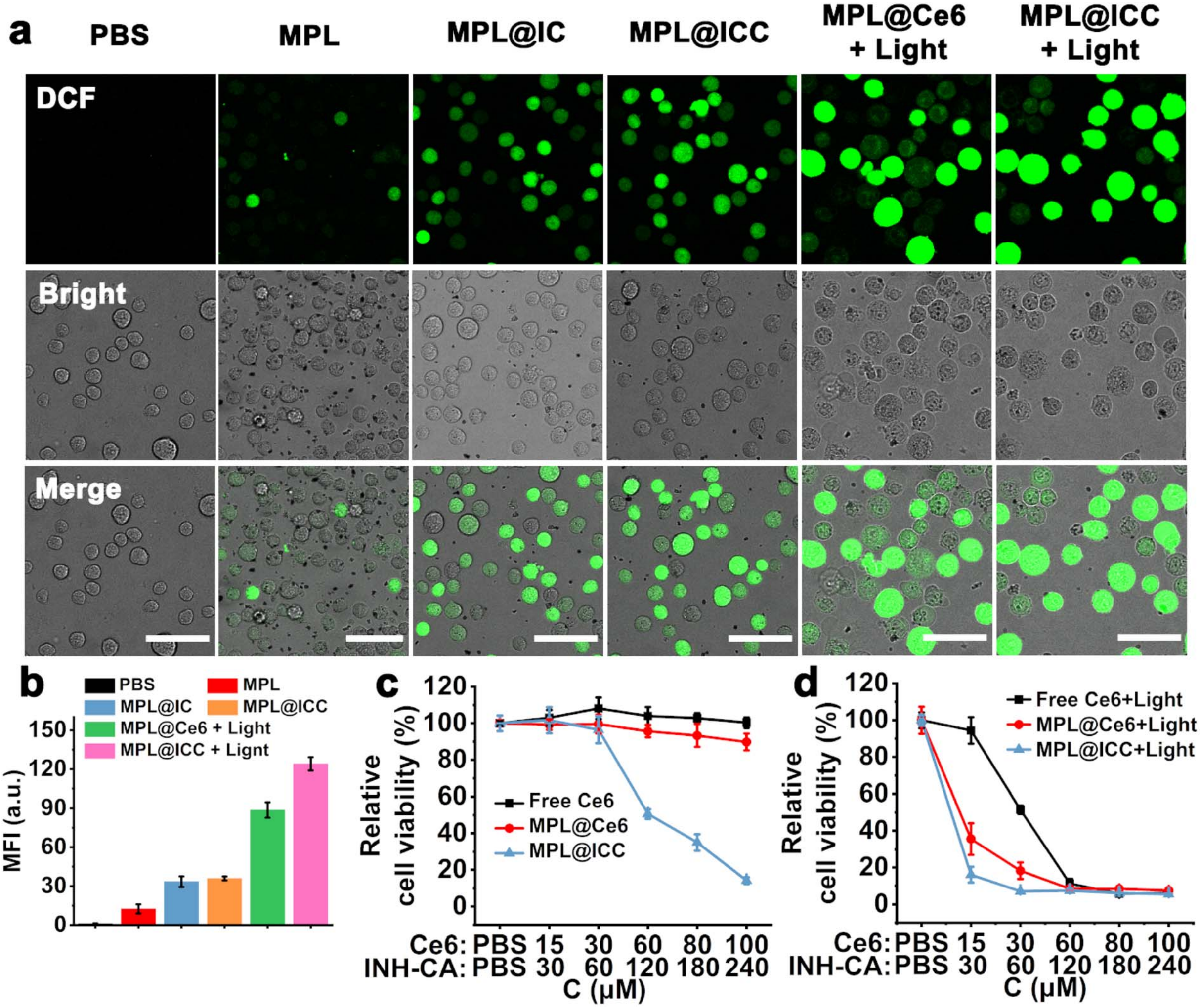

Fig. 4 (a) The oxidative stress in H22 cells with or without 660 nm light (1×10^5 cells per dish, DCF: Ex: 495 nm/Em: 530 nm). Scale bar: 50 μm. (b) The mean fluorescence intensity of (a) ($n = 3$). (c) The relative cell viabilities of HepG2 cells after incubation with free Ce6, MPL@Ce6, and MPL@ICC at various doses in the dark ($n = 5$, 5×10^3 cells per well). (d) The relative cell viabilities of HepG2 cells after incubation with free Ce6, MPL@Ce6, and MPL@ICC at various doses in light (660 nm, 5 mW cm^{-2}, 30 min, $n = 5$, 5×10^3 cells per well). Data are expressed as means ± SD.

therapeutic effect resulted in the death of nearly all tumor cells after exposure to light in the presence of low concentrations of MPL@ICC (Fig. 4d). Next, MPL@ICC was co-incubated with HL7702 cells for 24 h, and the results revealed that cytotoxicity was only observed in the presence of high concentrations of the nanoparticles (Fig. S31†).

Building upon the positive results above, the potential enhancement of MPL@ICC on the induction of ICD was investigated. Three effectors of ICD,[35] calreticulin (CRT) exposure, high mobility group box-1 (HMGB-1) release, and ATP release, were evaluated in H22 tumor cells following different treatments. In the treatment groups without light irradiation, there was no obvious CRT exposure after 3 h incubation due to insufficient free radical production (Fig. 5a). After 24 h, CRT exposure to cell membranes was observed in the MPL@IC and MPL@ICC treatment groups in contrast to the MPL treatment group. Given the lack of PDT, CRT exposure can only be attributed to ICD induced by Mn(III) mediated $^{\bullet}$R. In the treatment groups exposed to 3 h of light irradiation, CRT exposure was the weakest on the membrane of cells treated with free Ce6, which can be attributed to PDT alone. Cells treated with MPL@Ce6 displayed stronger CRT exposure, likely due to the enhanced cellular uptake and disruption of cellular redox balance by MnO_2 through Mn(II)-mediated Fenton-like reactions. The even stronger CRT exposure exhibited by the MPL@ICC treatment can therefore only be attributed to the additional Mn(III)-mediated $^{\bullet}$R generation, which further disrupts the cellular redox balance. The extracellular contents of HMGB-1 and ATP were examined and showed a similar trend to CRT expression (Fig. 5b and c, respectively). Based on all the results thus far, it can be concluded that MPL@ICC can successfully target hepatoma cells *in vitro* and induce a more robust ICD response by enhancing the PDT efficacy and generating $^{\bullet}$R.

Tumor cell rechallenge is the gold standard for detecting the ICD effect[36] *in vivo*. Therefore, to demonstrate the efficacy of MPL@ICC, we first treated H22 cells with MPL@ICC + light to obtain ICD cells. We then used these ICD cells as an immune

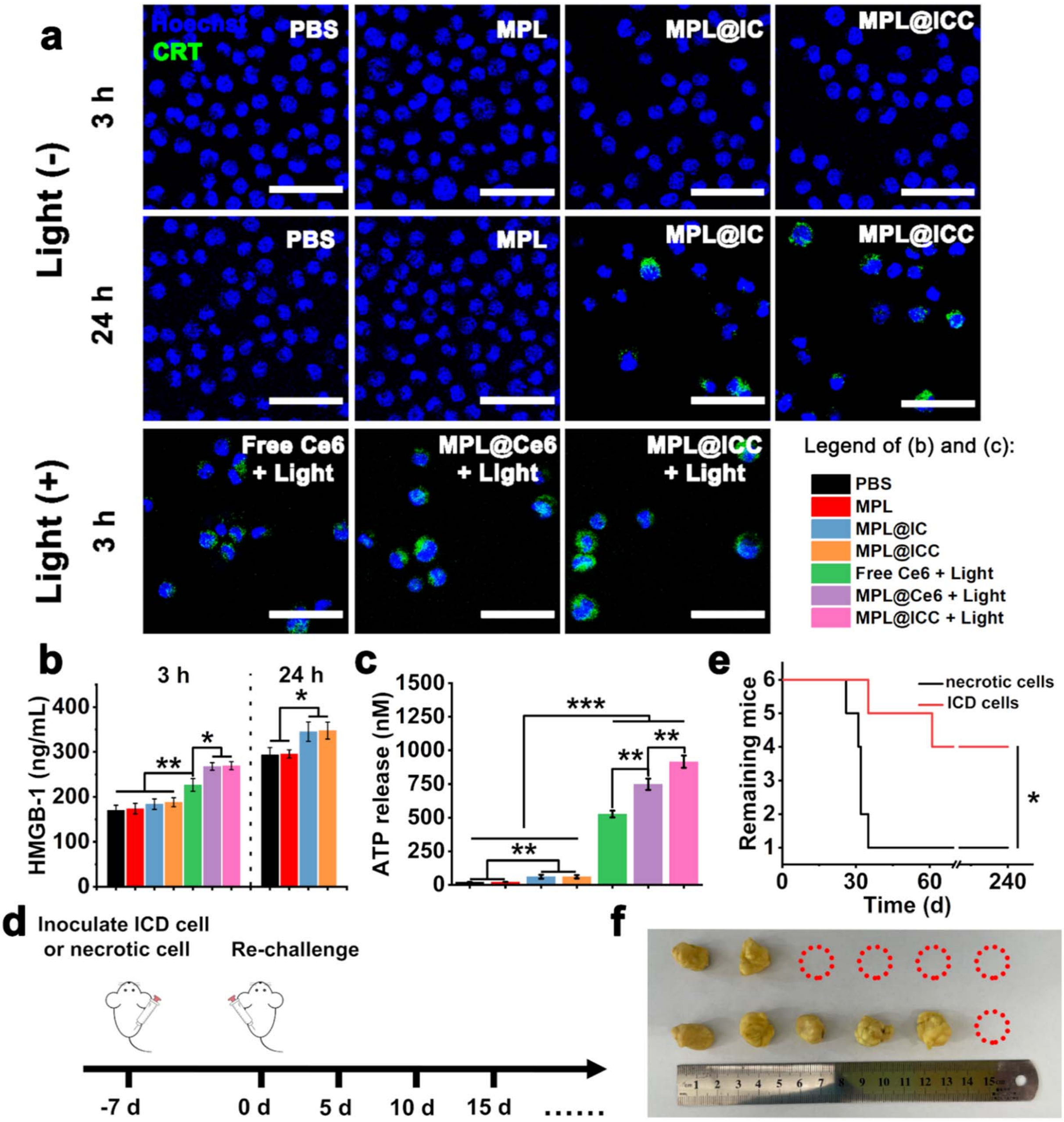

Fig. 5 (a) Calreticulin (CRT) exposure on the surface of H22 cells. (Anti-CRT antibody and FITC-labelled secondary antibody are used to label CRT. Hoechst 33258: Ex: 346 nm/Em: 460 nm; FITC: Ex: 488 nm/Em: 530 nm. scale bar: 50 μm.). (b) High Mobility Group Box-1 (HMGB-1) and (c) ATP release from H22 tumor cells after various treatments ($n = 3$). (I: PBS, II: MPL, III: MPL@IC, IV: MPL@ICC, V: free Ce6 + light, VI: MPL@Ce6 + light, VII: MPL@ICC + light). (d) The scheme of mice vaccinated. (e) Survival time of mice after being rechallenged by tumor cells ($n = 6$). (f) The photo of fixed tumor tissues (below: necrotic cells and above: ICD cells). Data are expressed as means ± SD. $^*p < 0.05$, $^{**}p < 0.01$ and $^{***}p < 0.001$.

vaccine and injected them into the right hindlimb of mice, while untreated necrotic H22 cells, obtained by freeze–thaw cycles, were inoculated into the right hindlimb of another group of mice as a control group. After 7 days, normal H22 cells were re-inoculated into the left hindlimb of mice and tumor growth was monitored (Fig. 5d). Compared with the control group, the survival time and the number of surviving mice in the test group significantly improved (Fig. 5e and f). These results confirmed that ICD obtained *via* treatment with MPL@ICC + light could induce an immune response in mice and thus MPL@ICC can function as an effective tumor vaccine.

Furthermore, an *in vivo* imaging system was used to study the drug distribution of the nanovaccine in H22 tumor-bearing mice at different times after tail vein injection. The fluorescence of Ce6 gradually increased at the tumor site and reached a peak around 12 h, which could still be observed even after 48 h (Fig. 6a and b). 12 h and 24 h after vein injection, the tumor and main organs were collected to observe the Ce6 fluorescence

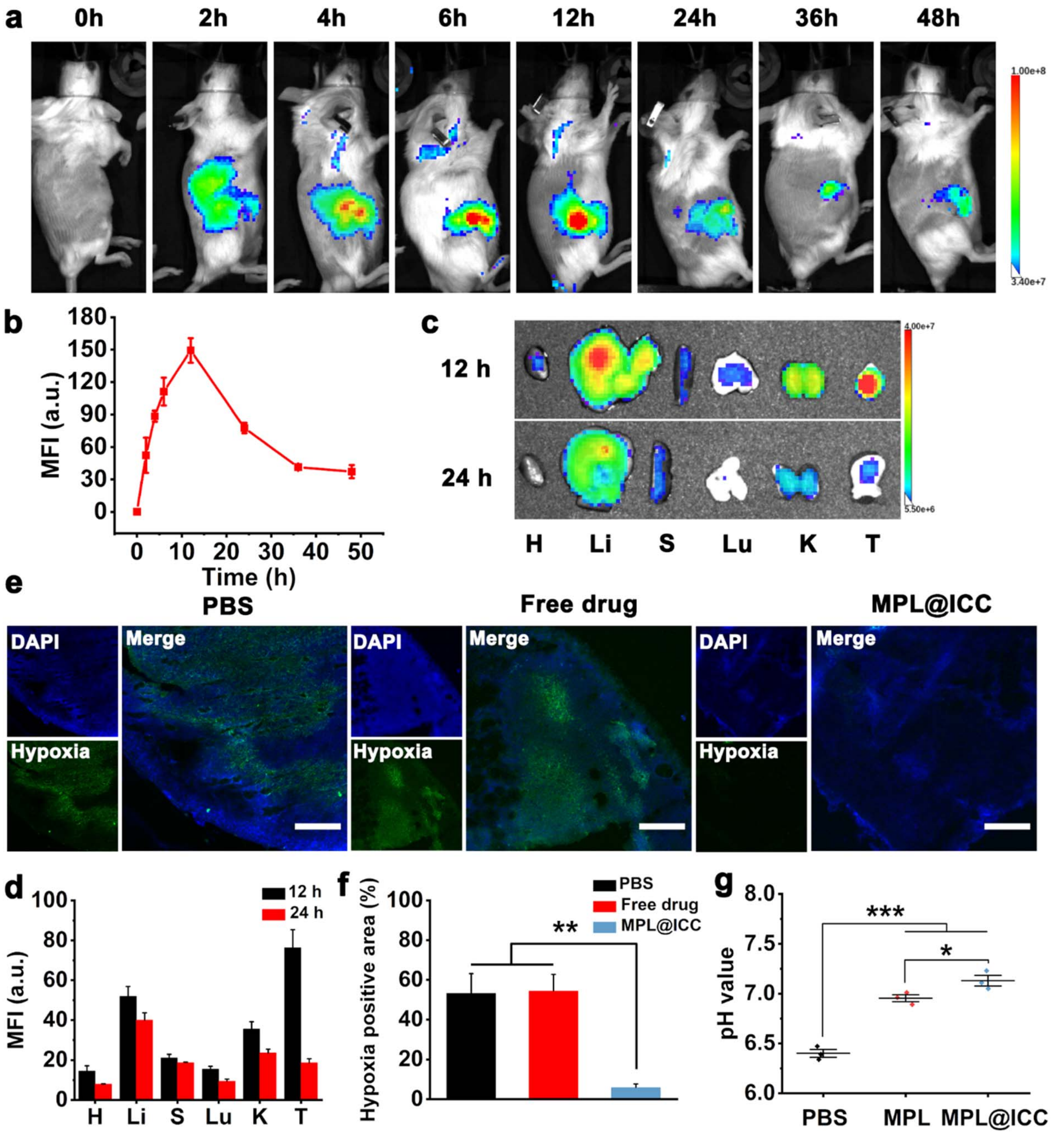

Fig. 6 (a) Real-time fluorescence images of H22 tumor-bearing mice after i.v. of MPL@ICC (fluorescence is attributed to Ce6, imaging mode: Ex: 675 nm/Em: Cy 5.5). (b) The corresponding mean fluorescence intensity of (a) ($n = 3$). (c) *Ex vivo* fluorescence images of major organs and tumors at 12 h and 24 h after intravenous injection of MPL@ICC (fluorescence is attributed to Ce6, imaging mode: Ex: 675 nm/Em: Cy 5.5). (d) The corresponding mean fluorescence intensity of (c) ($n = 3$). H: heart, Li: liver, S: spleen, L: lung, K: kidney, T: tumor. (e) Representative immunofluorescence images of the hypoxia area in tumors 12 h post injection of PBS, free drug, and MPL@ICC (DAPI: Ex: 360 nm/Em: 460 nm. Pimonidazole as a hypoxia probe, FITC-labeled anti-pimonidazole antibody shows fluorescence. Ex: 488 nm/Em: 530 nm.). Scale bar: 100 μm. (f) The percentage of the hypoxia positive area in tumors ($n = 3$). (g) pH of tumor tissue 24 h post injection of PBS, MPL, and MPL@ICC ($n = 3$). Data are expressed as means ± SD. $*p < 0.05$, $**p < 0.01$ and $***p < 0.001$.

signal. MPL@ICC had the highest mean fluorescence intensity in tumors 12 h after intravenous injection (Fig. 6c and d). All these results suggest that MPL@ICC exhibits increased tumor accumulation, which can be attributed to the EPR effect and targeting ability of MPL@ICC. Subsequently, a hypoxia probe was used to assess hypoxia relief at the tumor site 12 h after vein injection of the nanoparticles (Fig. 6e and f). The intravenously injected MPL@ICC group showed fewer hypoxia areas than the other groups, suggesting that MnO_2, which catalyses the decomposition of H_2O_2 to release O_2, alleviated hypoxia *in vivo*. The pH of tumor tissues was determined 24 h after intravenous injection of different nanoparticles. It was found that MPL and MPL@ICC upregulated the pH of tumor tissues (Fig. 6g).

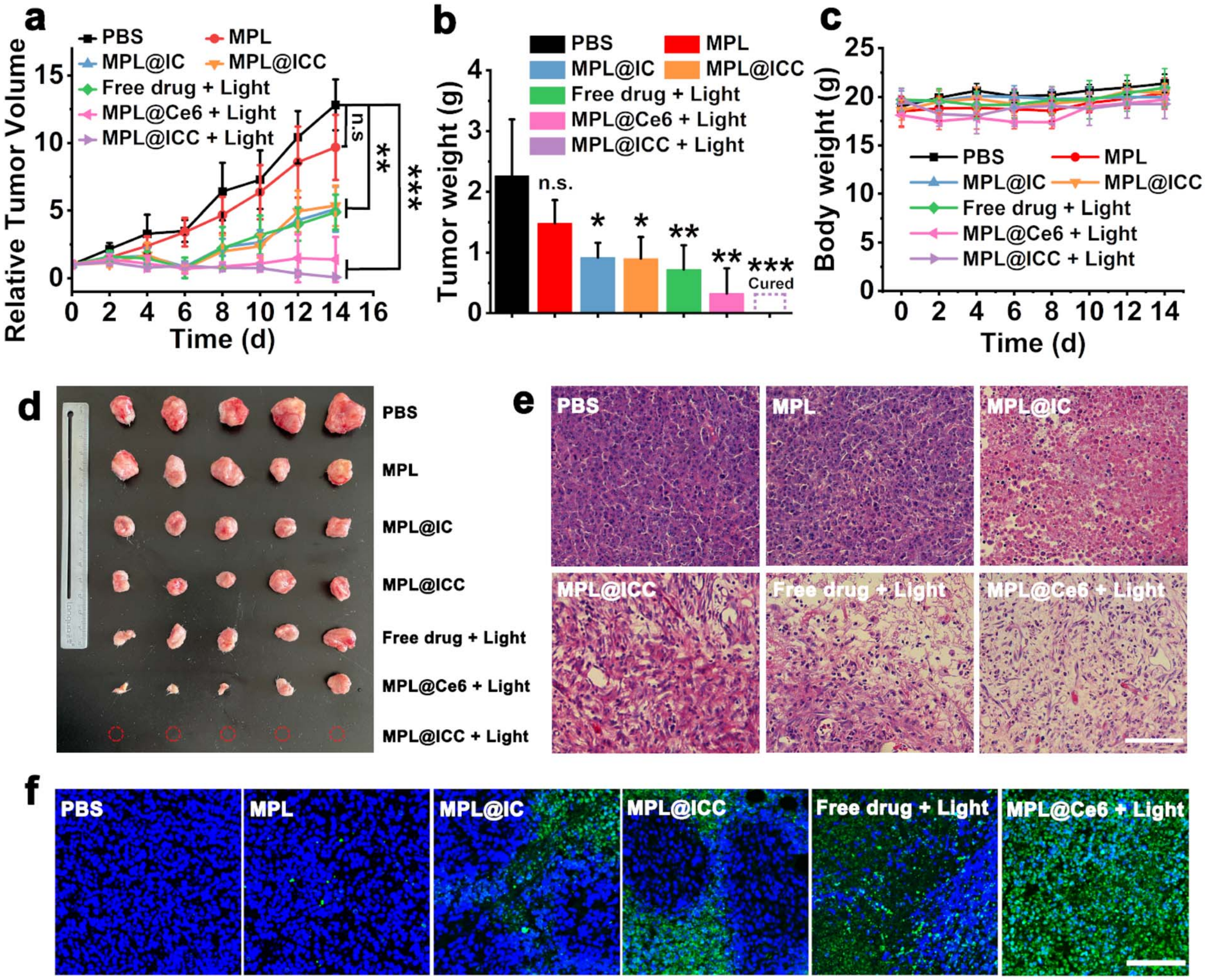

Fig. 7 (a) Tumor growth curves during the treatment and (b) average tumor weight after various treatments ($n = 5$). n.s.: not significant, $*p < 0.05$, $**p < 0.01$ and $***p < 0.001$. (c) Body weight change curves of mice during various treatments ($n = 5$). (d) The photo of the tumor at the end of treatment (red circles represent no tumor). (e) H&E staining of tumor slices after various treatments. (f) TUNEL staining of tumor slices after various treatments (nucleus stained with DAPI: Ex: 360 nm/Em: 460 nm. FITC-dUTP: Ex: 488 nm/Em: 530 nm). Scale bar: 100 μm data are expressed as means ± SD.

The therapeutic effects of nanoparticles were then evaluated in H22 tumor-bearing mice (Fig. 7a, b and 7d). When the tumor reached approximately 100–200 mm^3, H22 bearing mice were randomly divided into seven groups: PBS, MPL, free drug (Ce6 and INH-CA) + light, MPL@IC, MPL@ICC, MPL@Ce6 + light, MPL@ICC + light (MnO_2 = 9 mg kg^{-1}, Ce6 = 7.8 mg kg^{-1}, and INH-CA = 4.1 mg kg^{-1}). 660 nm light irradiation (0.4 W cm^{-2}) was applied at the tumor site for 5 min after 12 h injection. The MPL group exhibited a tumor suppressing effect consistent with previous studies. The tumor inhibition was significantly enhanced in the MPL@IC and MPL@ICC groups, which proves that Mn(III) mediated free radical production has a stronger antitumor effect than Mn(II) mediated CDT. Compared with the PBS group, the tumors in the free drug + light treated and the MPL@Ce6 + light treated showed rapid ablation after light therapy. Unfortunately, tumor recurrence occurred in both groups of mice, and was more rapid for the free drug + light group (Fig. 7a). MPL@ICC + light treatment completely eradicated the tumors, which may be attributed to the combined effects of PDT and free radicals (Fig. 7d and S32†). H&E and TUNEL staining assays were performed after various treatments. The result is given in Fig. 7e, which shows that destructive cell necrosis occurred in the group treated with MPL@Ce6 + light irradiation. Only a few apoptotic cells were observed in the light-treated free drug, MPL@IC, and the unlighted MPL@ICC groups. All these values were higher than the control and MPL groups, which did not show significant cellular damage. The results of TUNEL staining were consistent with the results of H&E staining (Fig. 7f). The biosafety of MPL@ICC was assessed by body weight changes and H&E staining of major organs. After various treatments, the body weight of the mice did not change significantly, and no obvious damage was observed in the major organs, indicating that MPL@ICC exhibits good biosafety (Fig. 7c and S33†).

Previous studies have shown that the hypoxic TME promotes the recruitment of regulatory T cells (Treg) to tumor sites and activates M2 macrophages to induce immunosuppression.[9,27,37] Considering that MPL@ICC can alleviate hypoxia and induce

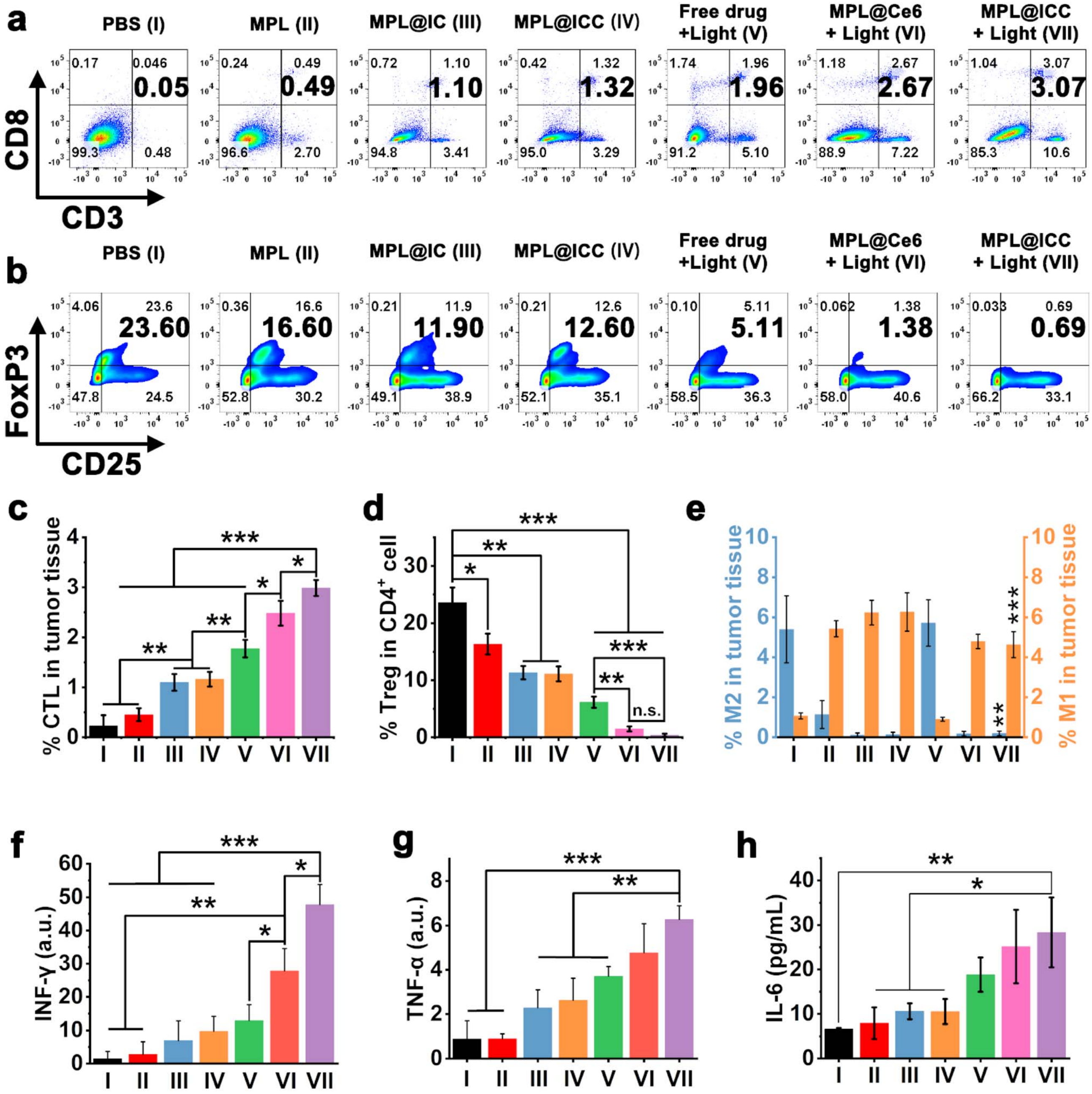

Fig. 8 (a) Representative flow cytometry charts of cytotoxic T lymphocytes (CTLs, $CD3^+CD8^+$) in tumors. (b) Representative flow cytometry charts of regulatory T (Treg, $CD25^+FoxP3^+$) in $CD4^+$ cells in tumors. (c) and (d) Quantification of CTLs and Treg in tumors analyzed by flow cytometry, respectively. Each group represents three independent mice ($n = 3$). (e) Quantification of M1 and M2 in tumors analyzed by immunofluorescence. Each group represents three independent mice ($n = 3$). (f) and (g) INF-γ and TNF-α in tumor tissue detected with RT-PCR (GAPHD as an internal reference gene), respectively. (h) The content of IL-6 in the blood of mice. I: PBS, II: MPL, III: MPL@IC, IV: MPL@ICC, V: free drug + light, VI: MPL@Ce6 + light, VII: MPL@ICC + light. Data are expressed as means ± SD. n.s.: not significant, $^*p < 0.05$, $^{**}p < 0.01$ and $^{***}p < 0.001$. IFN-γ: interferon-γ; TNF-α: tumor necrosis factor-α; IL-6: interleukin-6; GAPHD: glyceraldehyde-3-phosphate dehydrogenase.

TAA release from ICD tumor cells, the role of the nanovaccine in overcoming TME immune suppression and inducing systemic immune responses in mice was investigated. Tumors were collected on day 5 after the different treatments and the proportions of T cells were analysed by flow cytometry (Fig. 8a–d). There was only a small increase in cytotoxic T lymphocytes (CTLs) at the tumor site in mice treated with MPL (group II, about 0.45%) compared with the PBS group (group I, about 0.23%) (Fig. 8c). Notably, the tumors of the mice treated with MPL@IC (group III, about 1.10%) and MPL@ICC (group IV, about 1.16%) exhibited greater infiltration of CTL cells than that with MPL. These results suggest that Mn(III) mediated free radical production is more effective than Mn(II) mediated CDT in activating the immune system. After free drug + light (group V) treatment, CTLs in tumors were significantly increased (about 1.77%), indicating the potent role of PDT in inducing immune responses. After MPL@Ce6 + light (group VI) treatment, the infiltrated CTLs in tumors of mice increased to 2.48%, which can be attributed to the enhanced effect of MnO_2 on PDT by modulating the TME. More importantly, the MPL@ICC treatment group (group VII) showed the most CTL infiltration (about 2.99%), because PDT combined with the Mn(III) induced ICD strategy enhanced the immune response in mice *in vivo*. The trend of Treg cells infiltrating tumor tissue was opposite to that of CTLs (Fig. 8d), and large numbers of Treg cells infiltrated in PBS tumors were observed (about 23.58%). Compared with MPL treatment (16.35%), MPL@IC (about 11.33%) or MPL@ICC (about 11.10%) can more effectively reduce the number of Treg cells. And therapy with MPL@Ce6 (about 1.48%) or MPL@ICC (about 0.37%) more significantly reduced the number of immunosuppressive Treg cells in tumors than the free drug (about 6.16%). These remarkable effects can be attributed to the TME-modulating ability of MnO_2 and the release of relevant antigens resulting from photo- and Mn(III)-induced ICD of tumor cells. The changes in tumor associated macrophages (TAMs) on day 5 after the different treatments were determined using immunofluorescence. Compared with the PBS group, all mice treated with MnO_2 (MPL, MPL@IC, and MPL@ICC with/without light) exhibited significantly enhanced infiltration of M1-phenotype macrophages and reduced numbers of M2-phenotype macrophages (Fig. 8e and S34†). The phenotypes of M1/M2 macrophages in the tumor of mice treated with free drug + light have no significant change compared with that of the PBS group (Fig. 8e), which may be one of the important reasons for the rapid tumor recurrence after free drug + light treatment. These results indicate that treatment with MnO_2 alleviates tumor hypoxia resulting in a significant M2 to M1 polarization of TAMs in tumors, overcoming tumor tissue immunosuppression. In addition, we also detected the content of interferon-γ (IFN-γ), tumor necrosis factor-α (TNF-α) in tumor sites and interleukin-6 (IL-6) in mice blood, and the results showed an increase associated with CTLs and M1 macrophages (Fig. 8f, g and 8h), which also indicated the occurrence of an immune response in mice. In other words, the MPL@ICC nanovaccine can not only directly kill tumor cells in combination with PDT and free radicals, but also achieve immune killing induced by the photo- and Mn(III)-ICD strategies inside the tumor.

Conclusions

In summary, a highly effective cancer therapeutic nanovaccine MPL@ICC was rationally designed and fabricated based on ICD-inducing PDT, which greatly enhanced the PDT efficacy *via* Mn(III)-mediated ${}^{\bullet}R$ triggering ICD. The nanovaccine consisted of a nanovehicle of hollow MnO_2 coated by the pillar[6]arene$\supset$lactose-pyridine complex, an INH-CA prodrug, and Ce6. The coating of the complex endowed the nanovaccine with good hydrophilicity, size stability, and tumor targeting ability. The usage of INH in its prodrug state INH-CA prevented the reaction between INH and MnO_2 before MPL@ICC enters tumor cells. After MPL@ICC entered tumor cells, MnO_2 consumed GSH and converted H_2O_2 to O_2, which allowed the rapid release of INH-CA and Ce6. INH is then released from INH-CA due to the acidic TME, which enhanced the effect of PDT in combination with Ce6 to induce ICD due to hypoxia alleviation. Most importantly, the consumption of GSH and H_2O_2 by MnO_2 also increased the pH, which altered the TME to be more conducive to the existence of Mn(III). This facilitated Mn(III)-mediated generation of ${}^{\bullet}R$, which combined with the previously released INH, further potentiated immunogenic death of tumor cells. Furthermore, *in vivo* experiments indicated that H22 tumor-bearing mice were cured after treatment with the nanovaccine without reoccurrence in more than 300 days, indicating that a strong ICD effect was induced. The work provides a new strategy for designing highly efficient cancer therapeutic nanovaccines based on ICD-inducing cancer modalities, and exhibits tremendous potential for successful anti-tumor immunotherapy.

Data availability

All experimental and characterization data and detailed experimental procedures are available in the published article and ESI.†

Author contributions

Jiaxuan Li, Baifei Hu and Zelong Chen contributed equally to this work. Jiaxuan Li: investigation, methodology, formal analysis, conceptualization and data curation; Baifei Hu: investigation, methodology and data curation; Zelong Chen: investigation and visualization; Jiahui Li, Wenjuan Jin, Yi Wang, Yichen Wan: investigation; Yinghua Lv: methodology; Yuxin Pei: supervision, writing – original draft, funding acquisition; Hongtao Liu: supervision, writing – review and editing; Zhichao Pei: supervision, writing – review and editing, funding acquisition.

Conflicts of interest

The authors declare no conflict of interest.

Acknowledgements

This project was financially supported by the National Natural Science Foundation of China (21772157 and 21877088). The authors thank the Life Science Research Core Services (LSRCS) and College of Life Sciences, Northwest A&F University for helping with TEM (Kerang Huang), CLSM (Ningjuan Fan) and FCM (Min Zhou); the authors thank Dr Yincheng Chang at Beijing University of Chemical Technology for his help with ESR testing.

Notes and references

1 (*a*) C. L. Huang, L. Zhang, Q. Guo, Y. Y. Zuo, N. N. Wang, H. Wang, D. L. Kong, D. W. Zhu and L. H. Zhang, *Adv. Funct. Mater.*, 2021, **31**, 2010637; (*b*) C. Gao, C. Kwong,

Q. Wang, H. Kam, B. Xie, S. Lee, G. Chen and R. Wang, *ACS Nano*, 2023, **17**, 4034–4049.

2 (*a*) L. Qin, H. Zhang, Y. Zhou, C. S. Umeshappa and H. Gao, *Small*, 2021, **17**, e2006000; (*b*) J. Pan, Y. Wang, C. Zhang, X. Wang, H. Wang, J. Wang, Y. Yuan, X. Wang, X. Zhang, C. Yu, S. K. Sun and X. P. Yan, *Adv. Mater.*, 2018, **30**, 1704408.

3 (*a*) M. A. Islam, J. Rice, E. Reesor, H. Zope, W. Tao, M. Lim, J. X. Ding, Y. H. Chen, D. Aduluso, B. R. Zetter, O. C. Farokhzad and J. J. Shi, *Biomaterials*, 2021, **266**, 120431; (*b*) G. Z. Zhu, F. W. Zhang, Q. Q. Ni, G. Niu and X. Y. Chen, *ACS Nano*, 2017, **11**, 2387–2392.

4 (*a*) Y. H. Wang, Q. F. Zhao, B. Y. Zhao, Y. S. Zheng, Q. Y. Zhuang, N. S. Liao, P. Y. Wang, Z. X. Cai, D. Zhang, Y. Y. Zeng and X. L. Liu, *Adv. Sci.*, 2022, **9**, 2105631; (*b*) X. Yang, Y. Yang, J. Y. Bian, J. J. Wei, Z. Wang, Z. W. Zhou, Z. T. Li and M. J. Sun, *Nano Today*, 2021, **38**, 101109.

5 (*a*) H. Inoue and K. Tani, *Cell Death Differ.*, 2014, **21**, 39–49; (*b*) X. Zhao, K. Yang, R. Zhao, T. Ji, X. Wang, X. Yang, Y. Zhang, K. Cheng, S. Liu, J. Hao, H. Ren, K. W. Leong and G. Nie, *Biomaterials*, 2016, **102**, 187–197; (*c*) D. W. Zheng, J. L. Chen, J. Y. Zhu, L. Rong, B. Li, Q. Lei, J. X. Fan, M. Z. Zou, C. Li, S. X. Cheng, Z. Xu and X. Z. Zhang, *Nano Lett.*, 2016, **16**, 4341–4347.

6 (*a*) S. C. Formenti and S. Demaria, *J. Natl. Cancer Inst.*, 2013, **105**, 256–265; (*b*) Y. Min, K. C. Roche, S. Tian, M. J. Eblan, K. P. McKinnon, J. M. Caster, S. Chai, L. E. Herring, L. Zhang, T. Zhang, J. M. DeSimone, J. E. Tepper, B. G. Vincent, J. S. Serody and A. Z. Wang, *Nat. Nanotechnol.*, 2017, **12**, 877–882; (*c*) Z. Huang, Y. Wang, D. Yao, J. Wu, Y. Hu and A. Yuan, *Nat. Commun.*, 2021, **12**, 145.

7 (*a*) G. Lan, K. Ni, Z. Xu, S. S. Veroneau, Y. Song and W. Lin, *J. Am. Chem. Soc.*, 2018, **140**, 5670–5673; (*b*) L. Li, S. Yang, L. Song, Y. Zeng, T. He, N. Wang, C. Yu, T. Yin, L. Liu, X. Wei, Q. Wu, Y. Wei, L. Yang and C. Gong, *Theranostics*, 2018, **8**, 860–873; (*c*) M. Li, R. Guo, J. Wei, M. Deng, J. Li, Y. Tao, M. Li and Q. He, *Acta Biomater.*, 2021, **136**, 546–557; (*d*) C. Gao, Q. Wang, J. Li, C. H. T. Kwong, J. Wei, B. Xie, S. Lu, S. M. Y. Lee and R. Wang, *Sci. Adv.*, 2022, **8**, eabn1805.

8 (*a*) T. L. Aaes and P. Vandenabeele, *Cell Death Differ.*, 2021, **28**, 843–860; (*b*) R. D. Mule, A. Kumar, S. P. Sancheti, B. Senthilkumar, H. Kumar and N. T. Patil, *Chem. Sci.*, 2022, **13**, 10779–10785; (*c*) S. Sen, M. Won, M. S. Levine, Y. Noh, A. C. Sedgwick, J. S. Kim, J. L. Sessler and J. F. Arambula, *Chem. Soc. Rev.*, 2022, **51**, 1212–1233.

9 (*a*) S. D. Jo, G. H. Nam, G. Kwak, Y. Yang and I. C. Kwon, *Nano Today*, 2017, **17**, 23–37; (*b*) S. K. Daniel, K. M. Sullivan, K. P. Labadie and V. G. Pillarisetty, *Clin. Transl. Med.*, 2019, **8**, e10; (*c*) A. Facciabene, X. Peng, I. S. Hagemann, K. Balint, A. Barchetti, L. P. Wang, P. A. Gimotty, C. B. Gilks, P. Lal, L. Zhang and G. Coukos, *Nature*, 2011, **475**, 226–230.

10 (*a*) Y. Fan and J. J. Moon, *Vaccines*, 2015, **3**, 662–685; (*b*) S. Zhang, J. Wang, Z. Kong, X. Sun, Z. He, B. Sun, C. Luo and J. Sun, *Biomaterials*, 2022, **282**, 121433; (*c*) J. Zhou, L. Rao, G. Yu, T. R. Cook, X. Chen and F. Huang, *Chem. Soc. Rev.*, 2021, **50**, 2839–2891.

11 (*a*) M. Singh and D. O'Hagan, *Nat. Biotechnol.*, 1999, **17**, 1075–1081; (*b*) B. Pulendran, P. S. Arunachalam and D. T. O'Hagan, *Nat. Rev. Drug Discovery*, 2021, **20**, 454–475; (*c*) W. Lee and M. Suresh, *Front. Immunol.*, 2022, **13**, 940047.

12 (*a*) G. Yang, L. Xu, Y. Chao, J. Xu, X. Sun, Y. Wu, R. Peng and Z. Liu, *Nat. Commun.*, 2017, **8**, 902; (*b*) R. Liang, L. Liu, H. He, Z. Chen, Z. Han, Z. Luo, Z. Wu, M. Zheng, Y. Ma and L. Cai, *Biomaterials*, 2018, **177**, 149–160; (*c*) L. Hou, C. Tian, Y. Yan, L. Zhang, H. Zhang and Z. Zhang, *ACS Nano*, 2020, **14**, 3927–3940; (*d*) X. Chen, S. S. Gao, X. Wang, M. Y. Guo, Y. Y. Cui, Z. W. Chen, Y. Liu and Y. L. Wang, *Nano Today*, 2022, **46**, 101583; (*e*) H. Wang, Y. Liu, C. Xu, X. Wang, G. R. Chen, T. D. James, Y. Zang, J. Li, X. Ma and X. P. He, *Chem. Commun.*, 2018, **54**, 4037–4040.

13 (*a*) B. Ding, P. Zheng, F. Jiang, Y. Zhao, M. Wang, M. Chang, P. Ma and J. Lin, *Angew. Chem., Int. Ed.*, 2020, **59**, 16381–16384; (*b*) Y. Yang, Z. Gu, J. Tang, M. Zhang, Y. Yang, H. Song and C. Yu, *Adv. Sci.*, 2021, **8**, 2002667; (*c*) B. Ding, J. Yue, P. Zheng, P. Ma and J. Lin, *J. Mater. Chem. B*, 2021, **9**, 7117–7131; (*d*) X. J. Di, Z. C. Pei, Y. X. Pei and T. D. James, *Coord. Chem. Rev.*, 2023, **484**, 215098.

14 (*a*) E. Ember, S. Rothbart, R. Puchta and R. van Eldik, *New J. Chem.*, 2009, **33**, 34–49; (*b*) Y. Cheng, F. Yang, K. Zhang, Y. Zhang, Y. Cao, C. Liu, H. Lu, H. Dong and X. Zhang, *Adv. Funct. Mater.*, 2019, **29**, 1903850.

15 Y. Feng, Y. Liu, X. Ma, L. Xu, D. Ding, L. Chen, Z. Wang, R. Qin, W. Sun and H. Chen, *J. Nanobiotechnol.*, 2022, **20**, 193.

16 B. B. Ding, P. Zheng, J. Tan, H. Chen, Y. L. Bian, C. Z. Yang, P. A. Ma and J. Lin, *Chem. Mater.*, 2022, **34**, 1800–1808.

17 (*a*) B. Ding, P. Zheng, P. a. Ma and J. Lin, *Adv. Mater.*, 2020, **32**, 1905823; (*b*) J. Xu, W. Han, P. Yang, T. Jia, S. Dong, H. Bi, A. Gulzar, D. Yang, S. Gai, F. He, J. Lin and C. Li, *Adv. Funct. Mater.*, 2018, **28**, 1803804; (*c*) L. Tian, Q. Chen, X. Yi, J. Chen, C. Liang, Y. Chao, K. Yang and Z. Liu, *Small*, 2017, **13**, 1700640.

18 (*a*) B. B. Snider and R. B. Smith, *Tetrahedron*, 2002, **58**, 25–34; (*b*) G. W. Wang, T. H. Zhang, X. Cheng and F. Wang, *Org. Biomol. Chem.*, 2004, **2**, 1160–1163; (*c*) L. Qin, C. H. Huang, D. Xu, L. N. Xie, J. Shao, L. Mao, B. Kalyanaraman and B. Z. Zhu, *Free Radical Biol. Med.*, 2019, **143**, 232–239.

19 (*a*) W. Wu, Y. Yang, Z. Liang, X. Song, Y. Huang, L. Qiu, X. Qiu, S. Yu and W. Xue, *Nanoscale*, 2021, **13**, 11169–11187; (*b*) Y. Zhang, Q. Wang, Y. Ji, L. Fan, B. Ding, J. Lin and L. Wang, *Chem. Eng. J.*, 2022, **435**, 134869.

20 B. Ning, Y. Liu, B. Ouyang, X. Su, H. Guo, Z. Pang and S. Shen, *J. Colloid Interface Sci.*, 2022, **614**, 436–450.

21 (*a*) S. M. Webb, G. J. Dick, J. R. Bargar and B. M. Tebo, *Proc. Natl. Acad. Sci. U. S. A.*, 2005, **102**, 5558–5563; (*b*) A. S. Madison, B. M. Tebo, A. Mucci, B. Sundby and G. W. Luther 3rd, *Science*, 2013, **341**, 875–878.

22 (*a*) H. Lin, N. H. Szeinbaum, T. J. DiChristina and M. Taillefert, *Geochim. Cosmochim. Acta*, 2012, **99**, 179–192; (*b*) E. Hu, Y. Zhang, S. Wu, J. Wu, L. Liang and F. He, *Water Res.*, 2017, **111**, 234–243.

23 (*a*) M. E. Aikins, C. Xu and J. J. Moon, *Acc. Chem. Res.*, 2020, **53**, 2094–2105; (*b*) L. Zhang, K. Wang, Y. Huang, H. Zhang, L. Zhou, A. Li and Y. Sun, *Biomaterials*, 2022, **282**, 121411; (*c*) W. Qian, M. Zuo, G. Sun, Y. Chen, T. Han, X. Y. Hu, R. Wang and L. Wang, *Chem. Commun.*, 2020, **56**, 7301–7304.

24 (*a*) S. Liu, G. Feng, B. Z. Tang and B. Liu, *Chem. Sci.*, 2021, **12**, 6488–6506; (*b*) X. Li, Y. Zhang, X. Wu, J. Chen, M. Yang, F. Ma and L. Shi, *Small*, 2022, **18**, 2203100.

25 (*a*) W. Feng, S. Zhang, Y. Wan, Z. Chen, Y. Qu, J. Li, T. D. James, Z. Pei and Y. Pei, *ACS Appl. Mater. Interfaces*, 2022, **14**, 20749–20761; (*b*) H. Zhu, Q. Li, B. Shi, F. Ge, Y. Liu, Z. Mao, H. Zhu, S. Wang, G. Yu, F. Huang and P. J. Stang, *Angew. Chem., Int. Ed.*, 2020, **59**, 20208; (*c*) N. Song, Z. Zhang, P. Liu, D. Dai, C. Chen, Y. Li, L. Wang, T. Han, Y. W. Yang, D. Wang and B. Z. Tang, *Adv. Funct. Mater.*, 2021, **31**, 2009924.

26 (*a*) W. R. Wilson and M. P. Hay, *Nat. Rev. Cancer*, 2011, **11**, 393–410; (*b*) S. Chouaib, M. Z. Noman, K. Kosmatopoulos and M. A. Curran, *Oncogene*, 2017, **36**, 439–445; (*c*) C. Gao, C. H. T. Kwong, Q. Wang, H. Kam, J. Wei, Q. Chen, J. Zhang, S. M. Y. Lee, D. Gu and R. Wang, *Mater. Today*, 2022, **58**, 57–70.

27 L. Qin, C. H. Huang, L. Mao, B. Shao and B. Z. Zhu, *Free Radical Biol. Med.*, 2020, **154**, 1–8.

28 C. Vilchèze and W. R. Jacobs, *Antimicrob. Agents Chemother.*, 2012, **56**, 5142–5148.

29 G. W. Luther, *Geomicrobiol. J.*, 2005, **22**, 195–203.

30 (*a*) Y. Zhao, X. Zhang, C. Jia, J. Wu, H. Tang, J. Shang, C. Yuan, Y. Wang and P. Zhang, *Colloids Surf., B*, 2021, **201**, 111627; (*b*) E. S. Ilton, J. E. Post, P. J. Heaney, F. T. Ling and S. N. Kerisit, *Appl. Surf. Sci.*, 2016, **366**, 475–485.

31 (*a*) M. Li, J. Yu, X. Wang and Z. Yang, *Appl. Surf. Sci.*, 2020, **530**, 147230; (*b*) S. Yang, X. Song, P. Zhang and L. Gao, *J. Mater. Chem. A*, 2015, **3**, 6136–6145.

32 (*a*) J. E. Johnson, P. Savalia, R. Davis, B. D. Kocar, S. M. Webb, K. H. Nealson and W. W. Fischer, *Environ. Sci. Technol.*, 2016, **50**, 4248–4258; (*b*) P. Wuamprakhon, A. Krittayavathananon, N. Ma, N. Phattharasupakun, T. Maihom, J. Limtrakul and M. Sawangphruk, *J. Electroanal. Chem.*, 2018, **808**, 124–132.

33 F. Gao, Y. Tang, W. L. Liu, M. Z. Zou, C. Huang, C. J. Liu and X. Z. Zhang, *Adv. Mater.*, 2019, **31**, e1904639.

34 (*a*) M. Oishi, Y. Nagasaki, K. Itaka, N. Nishiyama and K. Kataoka, *J. Am. Chem. Soc.*, 2005, **127**, 1624–1625; (*b*) P. a. Ma, S. Liu, Y. Huang, X. Chen, L. Zhang and X. Jing, *Biomaterials*, 2010, **31**, 2646–2654.

35 (*a*) Z. L. Li, X. Q. Lai, S. Q. Fu, L. Ren, H. Cai, H. Zhang, Z. W. Gu, X. L. Ma and K. Luo, *Adv. Sci.*, 2022, **9**, 2201734; (*b*) Q. Chen, C. Y. Li and Q. B. Wang, *Small Methods*, 2023, 2201457; (*c*) X. Duan, C. Chan and W. Lin, *Angew. Chem., Int. Ed.*, 2019, **58**, 670–680.

36 (*a*) O. Kepp, L. Senovilla, I. Vitale, E. Vacchelli, S. Adjemian, P. Agostinis, L. Apetoh, F. Aranda, V. Barnaba, N. Bloy, L. Bracci, K. Breckpot, D. Brough, A. Buque, M. G. Castro, M. Cirone, M. I. Colombo, I. Cremer, S. Demaria, L. Dini, A. G. Eliopoulos, A. Faggioni, S. C. Formenti, J. Fucikova, L. Gabriele, U. S. Gaipl, J. Galon, A. Garg, F. Ghiringhelli, N. A. Giese, Z. S. Guo, A. Hemminki, M. Herrmann, J. W. Hodge, S. Holdenrieder, J. Honeychurch, H. M. Hu, X. Huang, T. M. Illidge, K. Kono, M. Korbelik, D. V. Krysko, S. Loi, P. R. Lowenstein, E. Lugli, Y. Ma, F. Madeo, A. A. Manfredi, I. Martins, D. Mavilio, L. Menger, N. Merendino, M. Michaud, G. Mignot, K. L. Mossman, G. Multhoff, R. Oehler, F. Palombo, T. Panaretakis, J. Pol, E. Proietti, J. E. Ricci, C. Riganti, P. Rovere-Querini, A. Rubartelli, A. Sistigu, M. J. Smyth, J. Sonnemann, R. Spisek, J. Stagg, A. Q. Sukkurwala, E. Tartour, A. Thorburn, S. H. Thorne, P. Vandenabeele, F. Velotti, S. T. Workenhe, H. Yang, W. X. Zong, L. Zitvogel, G. Kroemer and L. Galluzzi, *Oncoimmunology*, 2014, **3**, e955691; (*b*) J. Rios-Doria, J. Harper, R. Rothstein, L. Wetzel, J. Chesebrough, A. Marrero, C. Chen, P. Strout, K. Mulgrew, K. McGlinchey, R. Fleming, B. Bezabeh, J. Meekin, D. Stewart, M. Kennedy, P. Martin, A. Buchanan, N. Dimasi, E. Michelotti and R. Hollingsworth, *Cancer Res.*, 2017, **77**, 2686–2698.

37 D. Laoui, E. Van Overmeire, G. Di Conza, C. Aldeni, J. Keirsse, Y. Morias, K. Movahedi, I. Houbracken, E. Schouppe, Y. Elkrim, O. Karroum, B. Jordan, P. Carmeliet, C. Gysemans, P. De Baetselier, M. Mazzone and J. A. Van Ginderachter, *Cancer Res.*, 2014, **74**, 24–30.